NUMERICAL MODELING OF SOLID-LIQUID PHASE CHANGE IN A CLOSED 2D CAVITY WITH DENSITY CHANGE, ELASTIC WALL AND NATURAL CONVECTION

Jonathan Dallaire, Louis Gosselin*

Department of Mechanical Engineering, Université Laval, Quebec City, Quebec, Canada

Article accepté pour publication dans : International Journal of Heat and Mass Transfer, Volume 114, November 2017.

Abstract

In this paper, the solidification of water near its density extremum is simulated while taking into account the expansion of the phase change material resulting from the different density of the solid and liquid phases. A thermo-mechanical coupling is achieved through one of the boundaries of the cavity behaving as an elastic wall. A methodology is introduced in which the problem is adapted in order to be solved with commercial CFD software (ANSYS Fluent 17.0). It is shown that when both the density variations and interaction of the phase change material with its boundaries are taken into account, significant differences may be observed in the flow pattern and the thermal behavior of the system, as opposed to an approach where a free ceiling or a constant density would be used. The pressure buildup inside the cavity resulting from the expansion of the phase change material as it pushes against the elastic wall causes the melting temperature to drop, which hinders solidification. It is shown that this effect becomes more pronounced as the spring constant of the elastic wall increases. It is also demonstrated that, with the assumptions made in the present model, the pressure rise may significantly influence the buoyancy forces within the cavity and change the relative size of the two counter rotating convective cells in the liquid phase. In some cases, when the pressure rises very quickly, the density extremum in the cavity disappears which strongly changes the flow pattern, i.e., only a single counter-clockwise convective cell is present

* Corresponding Author: Louis.Gosselin@gmc.ulaval.ca; Tel.: +1-418-656-7829; Fax: +1-418-656-5343

in the cavity. This, in turn, changes the shape and position of the solidification front considerably.

Keywords:
density extremum; solid-liquid phase change; melting; solidification; variable density; mass conservation; thermo-mechanical coupling

Nomenclature

a_i	pressure dependent coefficient [-]
A_{mush}	mushy zone constant [N s m^{-4}]
c_p	specific heat at constant pressure [J kg^{-1} K^{-1}]
f	liquid fraction [-]
$\boldsymbol{F}$	external body force vector [N m^{-3}]
$\boldsymbol{g}$	gravitational acceleration vector [m s^{-2}]
h	sensible enthalpy [J kg^{-1}]
h_{sl}	latent heat of fusion [J kg^{-1}]
H	height of the cavity [m]
k	thermal conductivity [W m^{-1} K^{-1}]
L	length of the cavity [m]
p	pressure [N m^{-2}]
q	water density correlation parameter [-]
t	time [s]
T	temperature [K]
T_C	cold-side temperature [K]
T_H	hot-side temperature [K]
T_m	melting temperature [K]
$T_{\max}$	temperature at which density of water is maximum [K]
$\boldsymbol{u}$	velocity vector [m s^{-1}]

u_x x-component of the velocity vector [m s^{-1}]

w water density correlation parameter [K^{-q}]

x, y Cartesian coordinates [m]

Greek Symbols

β thermal expansion coefficient [K^{-1}]

ΔT_m melting temperature interval [K]

ε small number [-]

κ'' effective spring constant [Pa m^{-1}]

μ dynamic viscosity [N s m^{-2}]

ρ density [kg m^{-3}]

ρ_{max} maximum density of water [kg m^{-3}]

$\boldsymbol{\tau}$ viscous stress tensor [N m^{-2}]

Subscripts

i initial value

l liquid phase property

mush mushy region property

s solid phase property

w elastic wall property

1. Introduction

Solidification and melting in cavities has been used extensively as a benchmark problem, both numerically and experimentally to develop a better understanding of the heat transfer and fluid flow mechanisms during solid-liquid phase change [1–5]. In particular, the melting of gallium in a cavity [6] has been cited numerous times and served as a validation test case for many numerical models. Even in the last few years, phase change in rectangular cavities heated by the lateral walls has been the topic of many studies motivated by applications such as thermally-activated actuators [7–10], where the actuator is filled with a phase change material (PCM) and its ceiling wall can be

thermally activated to move as a result of the volumetric changes occurring during solidification or melting.

Modeling density variations during solid-liquid phase change, however, still presents a challenge. In the past years, mathematical and numerical models were developed by different authors in an attempt to take into account the expansion/shrinking of a phase change material during phase change. Amongst the different approaches to accommodate density and volume variations during phase change, the two simpler are the presence of an open surface through which mass may enter or leave the domain or a moving free surface [11]. A number of studies regarding the solidification and melting in an enclosure with natural convection and density variations have been published. For instance, Ho et al. [5] performed an experimental and numerical study of melting of n-octadecane in an enclosure with a moving ceiling. By varying the subcooling, as well as the Stefan and Rayleigh numbers over prescribed intervals in their experiments and numerical models, the authors developed a correlation to predict the height of the moving ceiling as a function of time. The authors mention, however, that by neglecting the weight and friction of the moving ceiling (i.e., thermo-mechanical coupling), the correlation always over predicted the correct position of the ceiling. Assis et al. [12] and Hosseinizadeh et al. [13] investigated melting of a PCM with natural convection in spheres, which is of interest, for example, in micro-encapsulated PCM applications. The authors opted for a free surface approach, where an air gap was left at the top of the spherical enclosure in order to allow the PCM to expand upon melting. Schmueli et al. [14] used a similar approach in their experimental and numerical study on melting with natural convection in a vertical cylinder. Hassab et al. [15] present two different models for the melting of wax: one that does not simulate volumetric expansion during melting and one that does take it into account. A comparison of the results of the two models showed significant differences between the two different approaches at low Biot number.

A few attempts have been made to study the thermo-mechanical coupling during solid-liquid phase change. Namely, Conti [17] introduced mathematical and numerical models in a study on the pressure dependence of the melting temperature for the one dimensional solidification problem of a PCM of finite length. In their work, Conti et al. [18] assessed the effect of the choice of the boundary condition (convective cooling or

prescribed heat flux) for a similar setup. In both works, the Clapeyron equation was used to derive an expression for the melting temperature as a function of pressure. The numerical results show that the transient behavior of the classical Stefan problem is replaced by an asymptotic behavior, which is caused by the pressure dependant melting temperature. Kowalczyk et al. [19] studied the phenomenon of high pressure induced freezing and thawing of water, which is of interest in the treatment of food and biotechnological substances with high hydrostatic pressures (HHP). In their model, the conservation equations for the enthalpy-porosity method are reformulated for a compressible PCM and the pressurization/decompression is achieved by adding or removing liquid water through a hole located at the top of the enclosure. The results show that the convective motion is strongly influenced by the compression of the PCM since liquid water at very high pressure does not exhibit any density extremum. Their results also show that natural convection has a significant impact on the solidification rate. In previous work [11], two thermo-mechanical coupling models were developed (elastic wall and air gap) and applied to the one dimensional problem of expansion during solidification of an incompressible PCM. Analytical expressions were derived for predicting important physical quantities at equilibrium, such as the position of the solidification front, the pressure rise, or the melting temperature.

In this work, the solidification of a PCM in a closed cavity is simulated while taking into account the density change during phase change. As a result of the expansion, the wall of the cavity is deformed and the pressure builds up, reducing the melting temperature and hindering phase change. The modeling and simulation of the PCM density variations and of the thermo-mechanical coupling are the main contributions of this paper. The goal of this paper is to provide a benchmark case study of solidification in a closed cavity in the presence of density change and buoyancy forces. It is worth noting that even though solidification of water (which expands upon solidification) is the focus of this study, the general methodology presented here could also be applied to the melting of other PCMs (i.e., a PCM that expands upon melting). Section 2 introduces the problem with its mathematical formulation. The numerical model and validation are detailed in Sections 3 and 4, respectively. Finally, the numerical results for two reference cases (free

ceiling and constant density) as well as three different stiffness (spring constant) of the elastic wall are presented in Section 5.

2. Mathematical formulation

The domain under study is shown in Fig. 1. It consists of a 2D rectangular cavity of initial height H_i and length L, filled with a PCM. In this study, it was assumed that the PCM was water, but other PCMs could eventually be simulated. The properties of water and ice [20] that were used are presented in Table 1. Note that all properties were assumed to have different values according to the phase of the PCM.

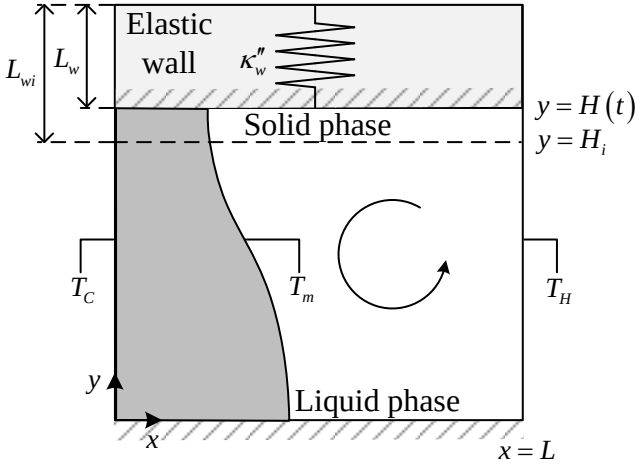

Figure 1

Table 1: Physical properties of water and ice

Property	Water	Units
ρ_s	918	kg m^{-3}
ρ_l	999.972	kg m^{-3}
c_{ps}	2025	J kg^{-1} K^{-1}
c_{pl}	4180	J kg^{-1} K^{-1}
k_s	2.19	W m^{-1} K^{-1}
k_l	0.58	W m^{-1} K^{-1}

T_m	273.15	K
ΔT_m	0.5	K
h_{sl}	333.4	kJ kg^{-1}
μ	Eq. (4)	kg m^{-1} s^{-1}

The PCM is initially liquid at a temperature T_i. Starting at time t = 0, the left-hand side wall is maintained at a temperature T_C which is below the melting point of the PCM, whereas the right-hand side is maintained at T_H, above the melting point. The horizontal walls are both adiabatic. Because of these boundary conditions, solidification takes place on the left-hand side wall and the frozen layer grows in time. Eventually, if solidification was allowed to go on for a sufficiently long period, the system would reach steady-state.

The governing equations that were solved in the PCM domain are the conservation of mass, momentum and energy implemented in ANSYS Fluent 17.0 [21]:

$$\frac{\partial \rho}{\partial t} + \nabla \cdot \left(\rho \boldsymbol{u} \right) = 0 \tag{1}$$

$$\frac{\partial}{\partial t}\left(\rho \boldsymbol{u} \right) + \nabla \cdot \left(\rho \boldsymbol{u} \otimes \boldsymbol{u} \right) = -\nabla p + \nabla \cdot \boldsymbol{\tau} + \rho \boldsymbol{g} + \boldsymbol{F} \tag{2}$$

$$\frac{\partial}{\partial t}\left(\rho h \right) + \nabla \cdot \left(\rho \boldsymbol{u} h \right) = \nabla \cdot \left(k \nabla T \right) \tag{3}$$

Note that the same equations were solved for both phases in the domain.

Compared to the majority of studies on solidification and melting, the fact that the density changes during phase change (in this study, the PCM expands upon solidification) means that the first term on the l.h.s. in Eq. (1) is non-zero in the region of the domain where the phase change occurs (i.e., phase front) even though ρ_s and ρ_l are constants. Therefore, there is a net velocity in the liquid phase at the interface due to the change of density. This insures mass conservation locally (at the solid-liquid interface or mushy region) as well as globally (in the domain).

In the conservation of momentum equation, a temperature dependant viscosity was used:

$$\begin{aligned} \mu\left(T \right) = & -3.020694 \times 10^{-8} T^3 + 2.603383 \times 10^{-5} T^2 \\ & -7.516218 \times 10^{-3} T + 7.280133 \times 10^{-1} \end{aligned} \tag{4}$$

This equation was obtained by fitting the data of table A.6 in [22] between 273.15K and 285K.

Equation (2) also includes two additional source terms. First, the term $\rho \boldsymbol{g}$ accounts for the buoyancy forces in the melt (natural convection). To determine the buoyancy forces, the correlation developed in [23] for the density of pure water as a function of temperature and pressure was used

$$\rho(T,p) = \rho_{\max}(p)\left[1 - w(p)\left|T - T_{\max}(p)\right|^{q(p)}\right] \tag{5}$$

This correlation allows the representation of the density extremum of water near 4 ºC, which results in different flow patterns than what would be observed if an alternative approach was used to describe the buoyancy forces, such as the Boussinesq approximation (see Chapter 4 in [24]). In Eq. (5), the pressure dependent quantities are given by:

$$\rho_{\max}(p) = \rho_{\max}(1)\left[1 + a_1(p)\right] \tag{6}$$

$$w(p) = w(1)\left[1 + a_2(p)\right] \tag{7}$$

$$T_{\max}(p) = T_{\max}(1)\left[1 + a_3(p)\right] \tag{8}$$

$$q(p) = q(1)\left[1 + a_4(p)\right] \tag{9}$$

$$a_i(p) = \sum_{j=1}^{3} a_{ij}(p-1)^j \tag{10}$$

where the pressure is expressed in bar. The following parameters at 1 bar were used: $\rho_{\max}(1) = 999.972\text{kg/m}^3$, $w(1) = 9.297173\times10^{-6}\text{K}^{-q}$, $T_{\max}(1) = 277.179325\text{K}$, and $q(1) = 1.894816$. The a_{ij} coefficients used in the present work yield a root mean square deviation $\sim 3.5\times10^{-3}$ kg/m^3 (check value 1040.2547 kg/m^3), see Table 1 in [23]. Since density variations of the melt with temperature are usually small (e.g., ~0.03% variation when comparing $\rho(T = 10\text{ºC})$ to $\rho_{\max}$ at a pressure of 1 bar) and assuming the PCM to be incompressible, the density of the liquid phase was assumed constant and equal to $\rho_{\max}(1)$ everywhere in the conservation equations, except in the buoyancy forces.

The second source term $\boldsymbol{F}$ is an external body force and inhibits fluid motion in the solid portion of the domain following the Carman-Koseny equation [25]:

$$\boldsymbol{F} = -\frac{(1-f)^2}{f^3+\varepsilon} A_{mush}\boldsymbol{u} \tag{11}$$

where the liquid fraction $f = 0$ in the solid phase, 1 in the liquid phase, and varies linearly between 0 and 1 over a small interval of temperature ΔT_m around the melting temperature T_m. In Eq. (11), a value of $\varepsilon = 0.001$ was used for all simulations (small number to avoid division by 0) and A_{mush} is the mushy zone constant. A wide range of values for the mushy zone constant A_{mush} were used in the past by various researchers. A recent study [26] showed that the effect of A_{mush} is critical in most simulations as the melting rate can either be overestimated or underestimated, which strongly influences the accuracy of the simulations. Their results also showed that A_{mush} and ΔT_m are not independent of one another when it comes to finding the correct values for the simulation results to match experimental results. For all numerical models used in the present study (including validation cases presented in Section 4), different combinations of both parameters were investigated in order to find optimal values. The final choice of these parameters is given for each model in the relevant sections of this paper.

Finally, the energy balance in Eq. (3) accounts for all relevant heat transfer mechanisms, including phase change. Due to the limitations of the software used to solve Eqs. (1)-(3) (see Section 3 below), it was decided to represent phase change via a modification of the specific heat so as to include latent heat rather than by solving explicitly for the liquid fraction. Different formulations are readily available for the apparent heat capacity method; see for example Ref. [27] for a discussion on the most widely used formulations and their limitations. It is worth mentioning that other formulations exist for this method. For instance, Ref. [26] introduced a method using a Gaussian function centered about T_m that ensures energy balance through the phase transition. Figure 2 shows the modified specific heat as a function of temperature that was used in the present paper. Over a small interval of temperature ΔT_m around the melting temperature, the value of c_p is increased in such a way that the integral under the

curve (shaded area in Fig. 2) is equal to the latent heat of fusion, i.e., $c_{pmush} = h_{sl}/\Delta T_m$. Since the equation for the conservation of energy is solved for the unknown enthalpy as opposed to the temperature, see Eq. (3), the modified specific heat depicted in Figure 2 is integrated with respect to temperature in order to calculate the energy variation within a given control volume at a given time step. This ensures that latent energy is properly accounted for during solidification. Note that in the mushy region, the other physical properties (k, ρ, and μ) are average properties. For example, the thermal conductivity in the mushy region is $k = (1-f)k_s + fk_l$.

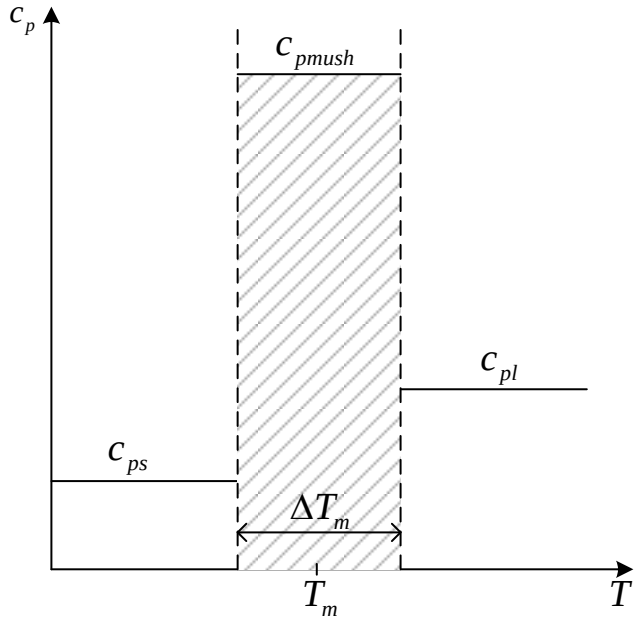

Figure 2

As the solidification takes place, the PCM expands. As mentioned in [11], there are different ways to accommodate volume change when modeling this type of problem, such as allowing excess mass to exit the domain via a permeable boundary or including a moving free surface in the domain. In this work, a closed container was modeled (see Fig. 1). The top surface was considered elastic, whereas the three other surfaces were infinitely rigid. During solidification, the elastic wall deforms and the height of the cavity evolves in time. Based on Hooke's law, the pressure buildup in the cavity can be calculated from the change in H over time [11]:

$$p(t) - p_i = \kappa_w'' \left[L_{wi} - L_w(t) \right] = \kappa_w'' \left[H(t) - H_i \right] \tag{12}$$

where κ_w'' is the effective spring constant of the elastic wall and can be linked to the geometry and mechanical properties of the elastic wall, see Appendix 1 in [11]. Assuming the PCM to be incompressible, the height of the cavity $H(t)$ is calculated by enforcing the conservation of the initial mass of the PCM.

In general, the increase in pressure affects the phase change temperature and to a lesser extent, the latent heat. In the present work, only the impact of pressure on the melting temperature was accounted for, i.e., the variation of latent heat was ignored. The Clapeyron relation allows expressing the melting temperature as a function of the pressure level in the domain as [11]:

$$T_m \left(p - p_i \right) = T_{mi} \exp\left[-\frac{1 - \rho_s / \rho_l}{\rho_s h_{sl}} \left(p - p_i \right) \right] \tag{13}$$

In the end, the governing equations (1)-(11) with the thermo-mechanical coupling of Eqs. (12)-(13) along with the initial and boundary conditions described at the beginning of this section constitute the present mathematical model.

3. Numerical implementation

The model described in Section 2 was implemented in ANSYS Fluent 17.0 which is based on the finite volume approach [28]. A mesh cut up the domain into small control volumes over which the governing equations are integrated, yielding a set of algebraic equations solved iteratively, time step by time step.

A series of adjustments and developments was needed in order to properly model the current problem within ANSYS Fluent 17.0:

(i) Properties in the mushy zone: One of the issues in phase change problems with density variation is the proper evaluation of physical properties within the mushy zone. In [29], it was showed that some of the properties appearing in Eqs. (1)-(3) are not the same in every term of the equations (within the mushy region), especially the density. However, in the software that was used, it is not possible to consider different property values in different terms of the governing equations. Therefore, it was decided to perform numerical

simulations for a pure PCM (water) with a narrow mushy zone in order to minimize the possible error induced when using the same properties in every term of the conservation equations.

(ii) Increase of volume: As mentioned above, as solidification takes place, the volume of the domain has to increase since $\rho_s < \rho_l$. At the beginning of each time step, the density field was integrated over the domain to determine the total PCM mass in the cavity. A new cavity height was calculated by adding liquid water at the top of the cavity until the total PCM mass was equal to the initial PCM mass. The position of the top boundary was then moved accordingly. This was accomplished by using the dynamic mesh tool provided by ANSYS Fluent 17.0 in conjunction with a "User Defined Function" (UDF) to perform the volume integral and calculate the required displacement of the top boundary. A layering technique was used to split the deforming layer of cells adjacent to the top boundary in order to preserve mesh quality.

(iii) Melting temperature: The phase change model available in the software did not allow the solidus and liquidus temperatures to change over the course of the simulation. However, in the present case, melting temperature is influenced by pressure which evolves in time, see Eq. (13). Therefore, it was necessary to deactivate the available phase change model and to implement a new one to be able to change the melting temperature. As mentioned in Section 2, an equivalent specific heat approach was thus used to account for the latent heat and was implemented with a UDF. In the momentum equations, the source terms blocking the velocity in the solid phase was also re-implemented with a UDF.

(iv) Thermo-mechanical coupling: At each time step, the mesh is deformed and the height of the domain is adapted to keep the total PCM mass constant. With the spring model introduced in Eq. (12), this results in an increase of pressure in the domain and as a consequence, in a change of the melting temperature. Therefore, the melting temperature is updated with Eqs. (12)-(13) inside each UDF. Accordingly, the specific heat versus temperature curve depicted in Fig. 2, as well as other temperature dependant properties calculated with UDFs,

were adapted so that the phase change temperature corresponded to its newly calculated value. Note that the actual pressure buildup was not used in the momentum equations directly as it constitutes a gauge that does not affect the pressure gradient.

The complete model was used to study a cavity with initial height $H_i = 0.15\text{m}$ and length $L = 0.15\text{m}$. The initial and boundary conditions are $T_i = 283.35\text{K}$, $T_C = 263.15\text{K}$, and $T_H = 283.35\text{K}$. Three values of the effective spring constant κ_w'' were investigated: 0.3 GPa/m, 3 GPa/m, and 30 GPa/m. In the dynamic mesh options, a split factor (ratio based) equal to 0.4 was used for the layering technique and the ideal cell height was set to 0.00075 m. For the numerical solution, the "SIMPLE" algorithm was chosen for the pressure-velocity coupling. Spatial discretization was performed with the "PRESTO!" algorithm for pressure, while the "QUICK" algorithm was used for momentum and energy. The transient formulation was set to first order implicit in all simulations. The following under-relaxation factors were used: 0.6 for pressure, 0.9 for density and body forces, 0.5 for momentum, and 0.1 for energy. Absolute convergence criteria varied between 1×10^{-4}-10^{-5} for continuity and momentum, and between 1×10^{-7}-10^{-8} for energy, depending on the effective spring constant. Both mesh and time step independences were thoroughly tested, which resulted in a final mesh of 150×200 control volumes and a time step of 1 s.

4. Validations

The model described in Sections 2 and 3 was validated step-by-step with four different cases documented in literature. Each test case aimed at validating a specific part of the model, each time adding new physics and new UDFs until the complete model was validated. First, the modified heat capacity approach was validated by comparing the results of the present model to the analytical solution presented in Example 11-3 in [30]. The problem considered is the solidification of a pure PCM (water) in a half-space with variable properties (except density). The PCM is initially liquid at $T_i = 273.2\text{K}$. At $t = 0$, the temperature at $x = 0$ is lowered to $T_C = 272.35\text{K}$ while the temperature at $x = L$ is

maintained at $T_H = 273.2\text{K}$. The top and bottom boundaries were defined as symmetry axes to make the problem one dimensional. The properties of water are given in Table 1 and the density used in the simulation was ρ_l. The temperature interval over which solidification takes place was $\Delta T_m = 0.1\text{K}$. The mesh consisted of 100 control volumes in the x direction and the time step was 100 s. Figure 3 shows the comparison between the analytical solution and the present model of the phase front position over time. The agreement is found to be excellent.

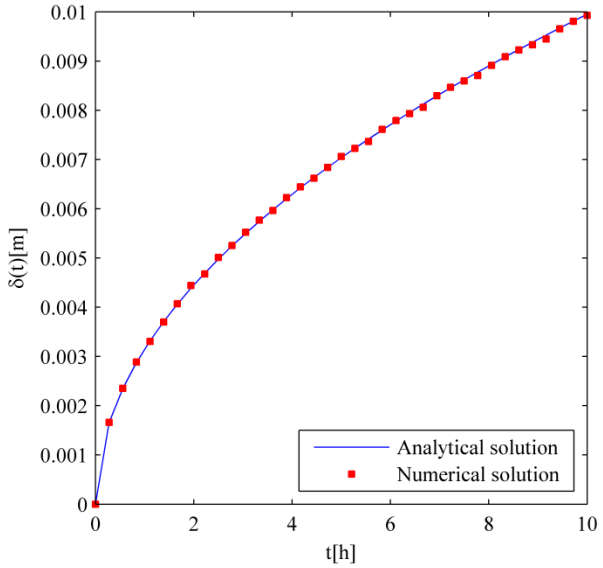

Figure 3

The second test case is the classic problem described in [6], i.e., phase change in a cavity filled with gallium with buoyancy forces. This test case aimed at validating the UDF that inhibits fluid motion in the solid phase, i.e., Eq. (11). The physical properties used in the simulation were $\rho = 6095\,\text{kg/m}^3$, $c_p = 381.5\,\text{J/kg}\cdot\text{K}$, $k = 32\,\text{W/m}\cdot\text{K}$, $\mu = 0.00181\,\text{kg/m}\cdot\text{s}$, $T_m = 302.93\text{K}$, $\Delta T_m = 0.6\text{K}$, and $h_{sl} = 80160\,\text{J/kg}$. In addition, the Boussinesq approximation was used instead of Eq. (5) to calculate the buoyancy forces in the melt with a thermal expansion coefficient $\beta = 0.00012\text{K}^{-1}$. The mushy zone constant was $A_{mush} = 1\times10^6\ \text{N}\cdot\text{s/m}^4$. The cavity dimensions as well as the boundary and initial conditions were chosen in order to match as closely as possible the experimental setup for

the cavity with an aspect ratio $A = 0.714$ described in [6]. The position of the solid-liquid interface is shown in Fig. 4 at different times and the numerical results are in good agreement with the experimental results from [6], given the uncertainties of the model and experiment results.

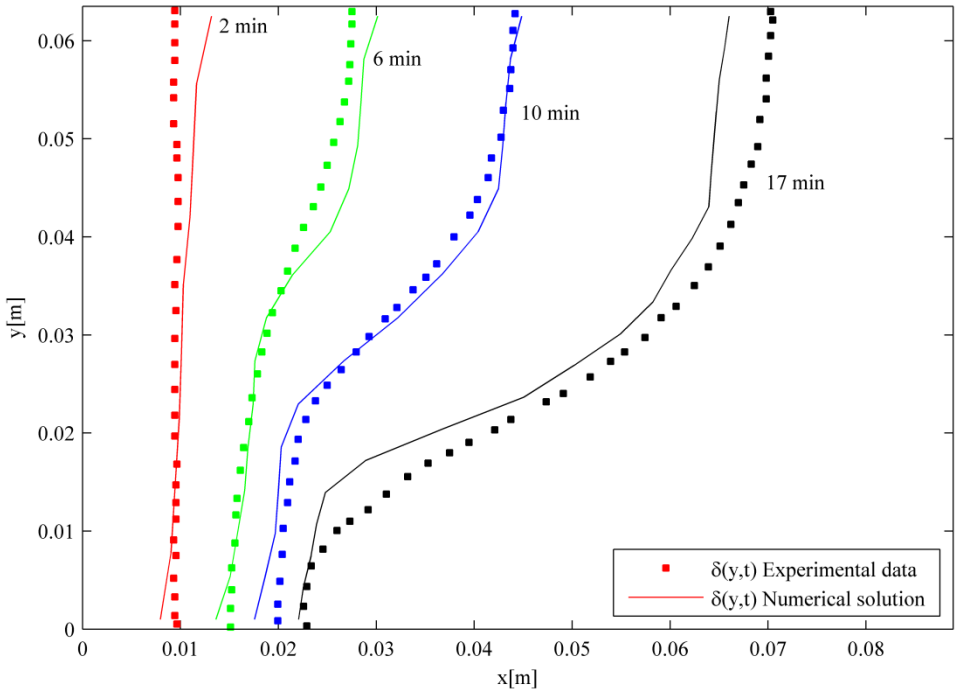

Figure 4

The third test case served to validate the UDFs for calculating the different physical properties of the PCM, as well as the buoyancy forces from Eq. (5). The problem is that of solidifying water in a cavity near its density extremum. Since water density is maximal near 4 ºC at atmospheric pressure, the flow pattern inside the cavity will consist in two counter-rotating natural convection cells. A small clockwise circulation cell will develop at the bottom of the cavity as cold water near the solidification front rises, while a large counter-clockwise circulation cell will develop in the remaining part of the cavity. This phenomenon and the experimental setup used for the validation of the numerical model (experiment A) are described in [31]. The properties of water used in the simulation are found in Table 1 and the value of the mushy zone constant that yielded the best results was $A_{mush} = 1 \times 10^7 \ \mathrm{N \cdot s/m^4}$. The mesh

consisted in 300 control volumes in the x direction and 200 control volumes in the y direction and the time step was 1 s. Further mesh or time step refinements did not result in significant changes of the solution. Even though the top surface did not move during this simulation, the boundary condition at the top surface for the momentum conservation equation was adapted to represent a free surface similarly to the experimental setup. Instead of a no slip boundary condition ($u_x = 0$), a no shear boundary condition was imposed ($\partial u_x / \partial y = 0$). The position of the solid-liquid interface at different times is depicted in Fig. 5. The numerical results at 15 and 60 minutes obtained by Scanlon and Stickland [32] were also shown for the sake of comparison. As can be seen in Fig. 5, the numerical results of the present work are in good agreement with both the experiment described in [31] and the numerical results presented in [32]. The small discrepancies can be explained by the differences between the numerical and experimental setups. Namely, there was a small adaptation period ~1-4 minutes before the temperature on the left-hand side of the cavity reached its prescribed value during the experimental measurements, but it is unclear whether the experimental time t=0 was before or after this adaptation period, which could explain why the numerical solution is slightly behind the experimental solution (especially at early times). In addition, the exposure time to produce the photos of the experimental phase change front was ~100 s, which makes it hard to define the position of the phase front with precision. Note that the top and bottom boundaries are assumed to be perfectly adiabatic in the numerical simulation, which is impossible to obtain in reality. As explained in [33], conduction in the x direction through the bottom boundary of the container in the experiment can cause the $T = T_{\max}$ isotherm to move to the right which results in a larger circulation cell in the bottom-left corner of the cavity. This, in turn, influences the shape and position of the solid-liquid interface. It is noteworthy to mention that according to the collection of experimental data presented in [20], some of the properties of fresh-water ice reported in literature show a wide range of different values at a given temperature, especially the specific heat and the thermal conductivity. The sensitivity of the numerical results to both c_{ps} and k_s was investigated, and it was found that they have a significant impact on the position of the solid-liquid interface at a given time. For instance, the choice of a slightly lower value for c_{ps} and

higher value for k_s (while remaining within the reported interval for each property) resulted in a better prediction of the interface position when compared to the experimental data.

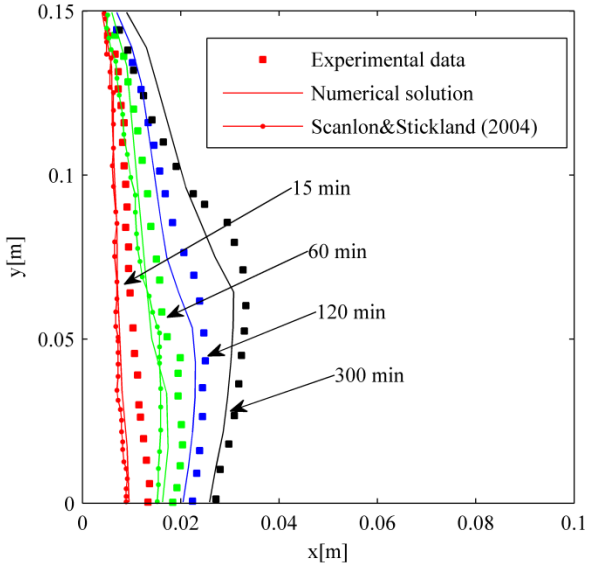

Figure 5

Finally, the present model was compared with the 1D solution presented in [11] for phase change with density change and thermo-mechanical coupling (labeled "Reference case" in Fig. 6). The features that were validated with this test case were the new UDF that calculates $H(t)$ (dynamic mesh), as well as the new portions of code added to existing UDFs for all calculations related to the thermo-mechanical coupling. The code developed in previous work was reused for this test case for the same system described in Section 4 of [11], with the exception that $\Delta T_m = 0.5\text{K}$. The reason for this modification is that the temperature interval used in previous work was too small for the present model with the modified specific heat approach. Since both the initial condition T_i and boundary condition T_H were defined as $T_{mi} + \Delta T_m/2$, both models needed to be compared with the same value of ΔT_m. Note that there is no mushy zone constant for this validation case, since the velocity in the mushy zone and in the melt is calculated directly from the continuity equation. The mesh used with the present model was made out of 300 control volumes and the time step was 90 s. The evolution of the position of the solid-

liquid interface and of the melting temperature are reported in Fig. 6 for $\kappa_w'' = 0.3\mathrm{GPa/m}$, in which it can be seen that both models yield similar results.

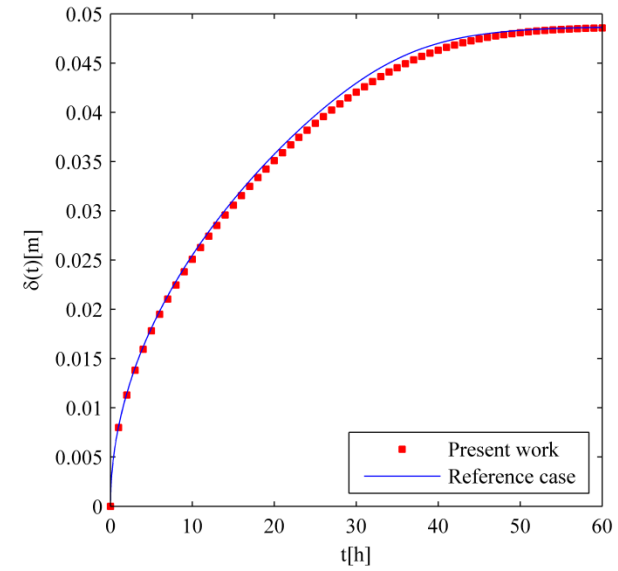

a)

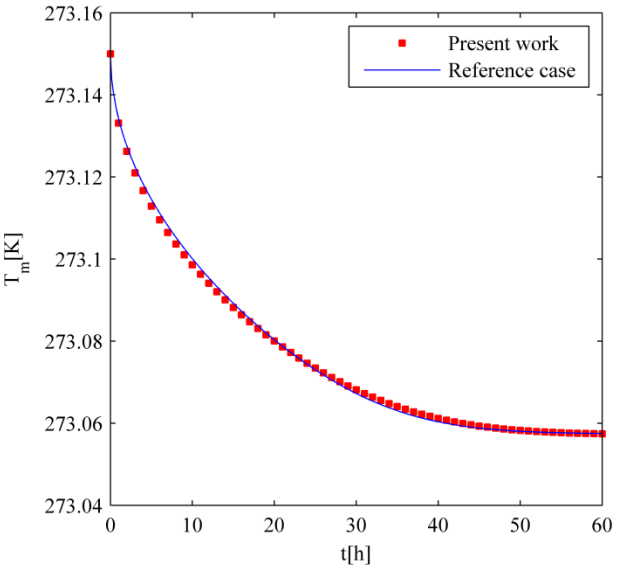

b)

Figure 6

5. Results and discussion

In this section, the numerical results obtained with the complete model described in Sections 2 and 3 are presented. Three different values of the effective spring constant were investigated, namely κ_w''=0.3 GPa/m, 3 GPa/m, and 30 GPa/m. Two additional cases were also simulated for the sake of comparison. In the first case, it was assumed that the PCM was not confined by an elastic wall, i.e., the top surface was considered as a free ceiling with κ_w''=0 GPa/m, whereas in the second case, it was assumed that $\rho_s = \rho_l$ (equal to the average density of the solid and liquid phases). The properties of water used for all cases are found in Table 1, with a mushy zone constant $A_{mush} = 1\times10^7\ \mathrm{N\cdot s/m^4}$. In order to help understand the overall behavior of the problem studied in this work, a qualitative description of the solidification process is first presented in Section 5.1, where the effect of the confinement of the PCM on the flow pattern inside the cavity is discussed. Then, some critical parameters related to the thermo-mechanical coupling were selected and are presented in Section 5.2. Finally, the thermal behavior of the system is analyzed in Section 5.3.

5.1 Effect of the PCM confinement on the flow inside the cavity

Due to the resemblance of the problem studied in the present paper with the third validation case, it is expected that the overall behavior of the system will be similar as long as the pressure rise inside the cavity remains small, which will occur either at early times or when the effective spring constant is very small. At the beginning of the cooling process, the dominant mode of heat transfer is conduction. The initial motion of the liquid phase is driven by the cold water flowing downward adjacent to the cold wall on the left-hand side and then extends to the remainder of the cavity to form a large counter-clockwise convective cell. As the PCM solidifies, a small clockwise convective cell may develop at the bottom of the cavity near the solid-liquid interface as lighter cold water at $T < T_{\max}$ rises near the solidification front. The remaining portion of the cavity is occupied by a larger counter-clockwise convective cell driven by lighter hot water at $T > T_{\max}$ rising up next to the right-hand side of the cavity maintained at T_H (see for

example Fig. 7). The same behavior was obtained both in experiments [31] and numerical simulations [32], [34] of unconstrained PCM.

To demonstrate the effect of the confinement of the PCM (and the pressure rise in the cavity) on the general behavior of the system, three different values of κ_w'' were used in the simulations. Figure 7a shows contours of the stream function with κ_w''=0.3 GPa/m after allowing the solidification process to go on for 300 min. On the left-hand side of the cavity, a layer of ice has formed. Note that in Figs. 7 to 9, the position of the solid-liquid interface is indicated by a solid black line. It can be observed that the layer of ice in Fig. 7 is thicker in the region adjacent to the cold convective cell near the bottom of the cavity, as can be seen in Fig. 7b, which shows contours of temperature in the cavity. In the liquid portion of the cavity, the two distinct counter-rotating convective cells are clearly visible. For such a small value of κ_w'' the pressure rise within the cavity is very small. In this case, the variation of the height of the cavity at the end of the simulation is ~2 mm. Using the thermo-mechanical coupling equation for pressure, i.e., Eq. (12), it is possible to estimate that the pressure rise is ~600 kPa. Therefore, the overall behavior of the system (flow pattern, solid-liquid interface position, melting temperature, etc.) is close to that of an unconstrained PCM (free ceiling).

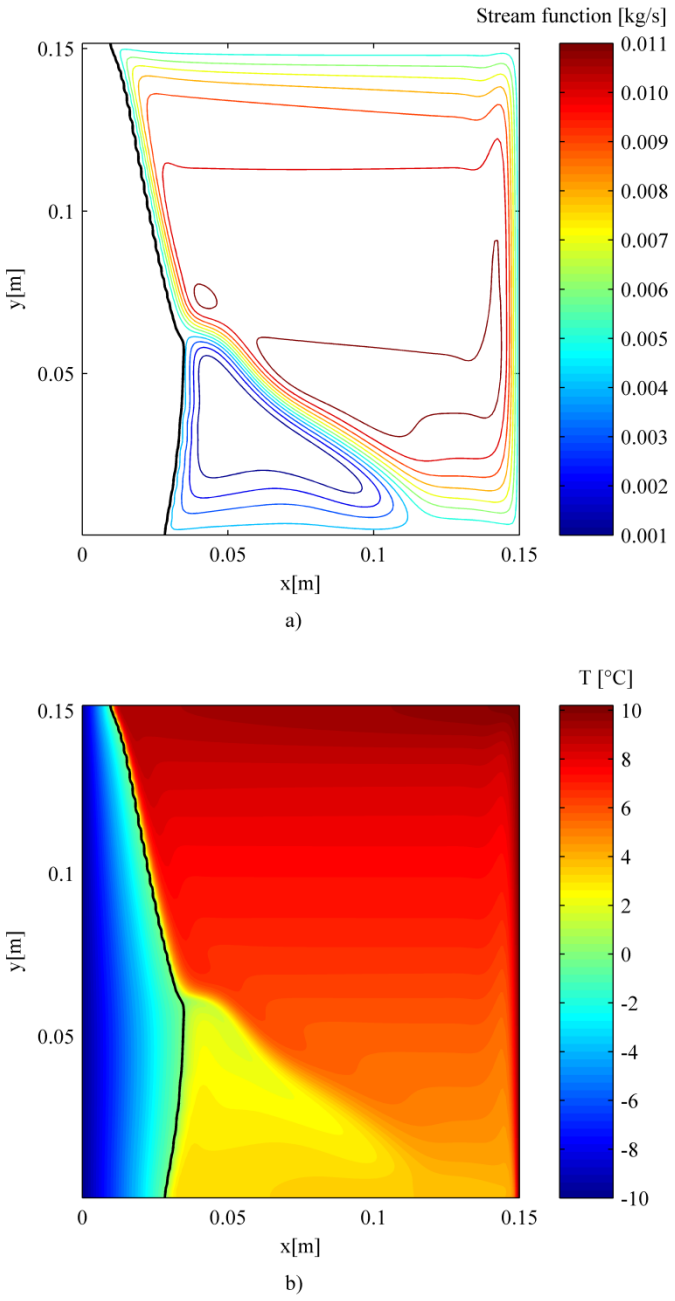

Figure 7

Figures 8a and 8b depict contours of the stream function and temperature for the second value of the effective spring constant (κ_w''=3 GPa/m) at t=300 min, respectively. In this case, the pressure build up is much higher (see Section 5.2). Although the overall behavior is similar, some differences appear in the flow pattern, as well as in the shape and position of the solidification front. For instance, the cold clockwise convective cell at

the bottom of the cavity is much smaller in this case, which makes the ice layer thicker on a smaller portion of the cavity in the y direction. This is a direct consequence of the pressure dependent density in the buoyancy forces, see Eq. (5). As the pressure inside the cavity increases, the density extremum in the liquid phase occurs at a temperature closer to the melting temperature, which causes the clockwise convective cell to slowly vanish. It addition, since the melting temperature of the PCM is smaller in this case, the solidification was not allowed to progress as much, which results in an overall slightly thinner layer of ice next to the cold wall of the cavity (this will be shown in Section 5.3).

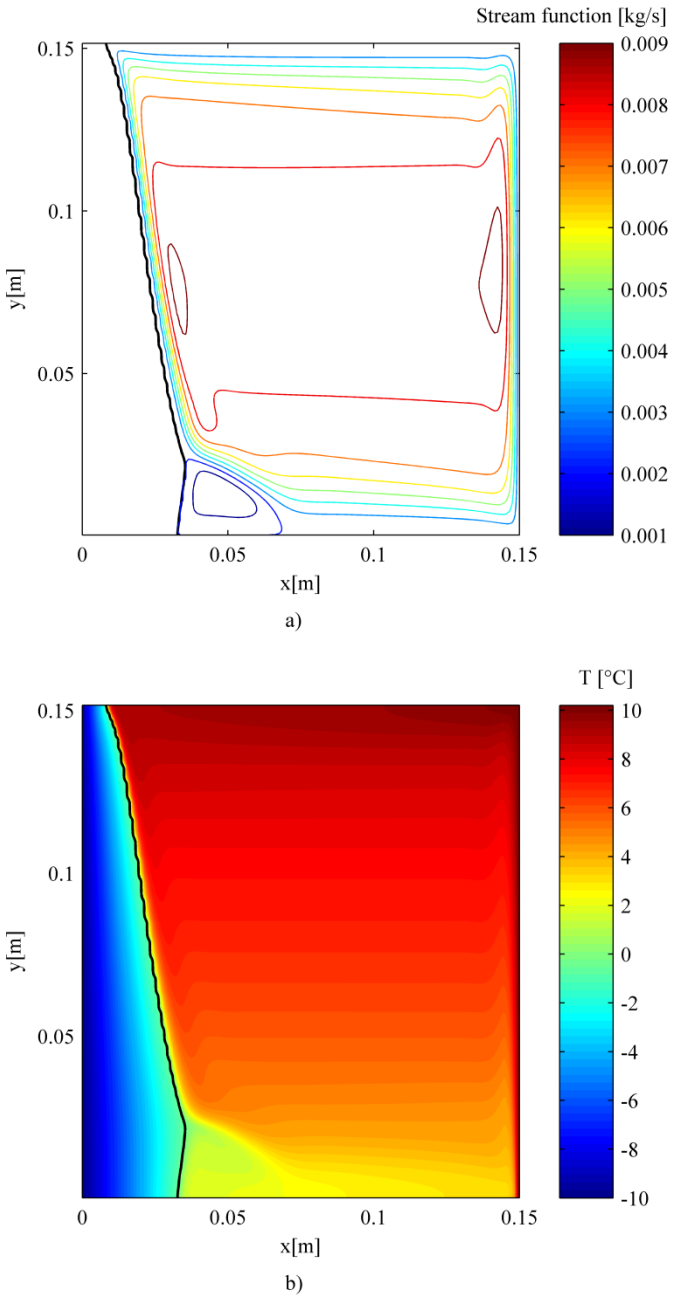

Figure 8

The highest value of the effective spring constant (κ_w''=30 GPa/m) yields quite a different behavior compared to the smaller values due to the very high pressure inside the cavity, as seen in Figs. 9a and 9b which show contours of the stream function and temperature at t=300 min. At the beginning of the simulation, the pressure level rises very quickly as the PCM pushes against the very stiff elastic wall and the melting

temperature drops accordingly. In fact, the pressure rise in this particular case occurs so rapidly that the density extremum quickly vanishes from the cavity during the simulation (i.e., $T_{\max}$ does not lie between T_m and T_H at these pressure levels, as will be shown in Section 5.2) and there is only one large counter-clockwise convective cell. Therefore, the shape of the solid-liquid interface is much different than in the previous cases: the layer of ice is thinner near the top of the cavity and grows thicker as the water cools down near the interface, until the ice layer reaches its maximum thickness at the bottom of the cavity. Another consequence of the pressure rise is that the solidification is slowed down considerably and the overall layer of ice is much thinner.

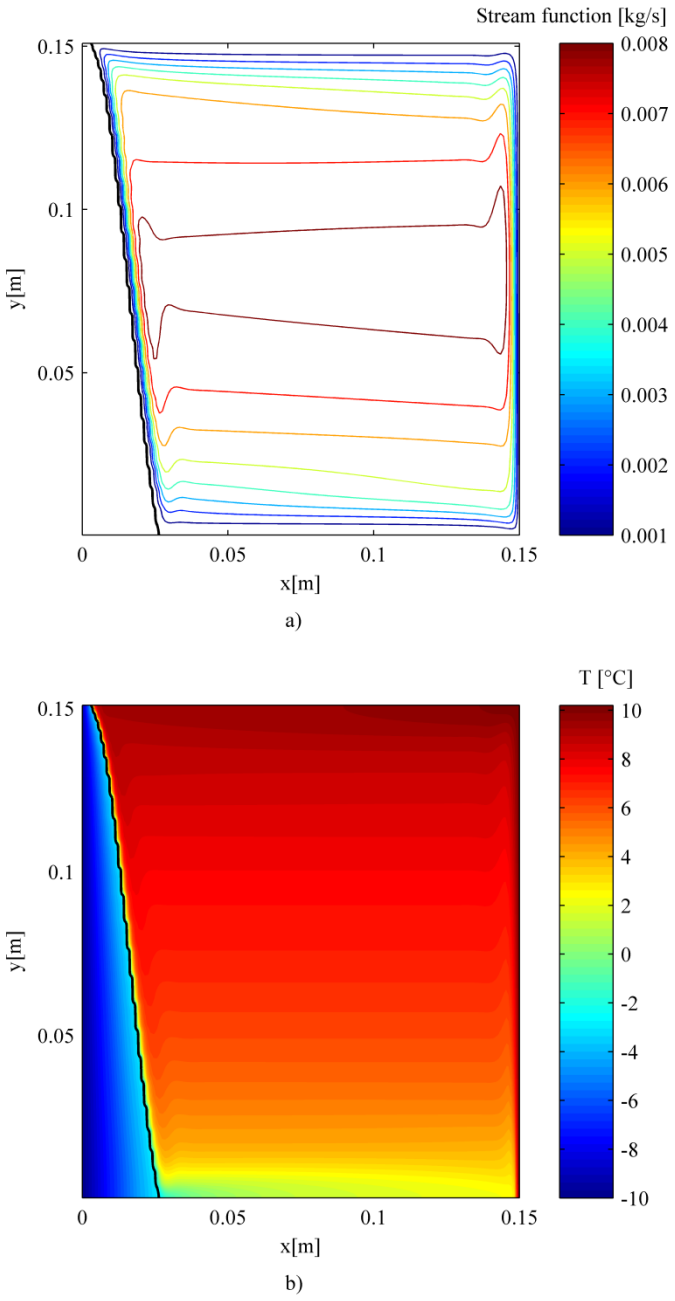

Figure 9

5.2 Pressure build-up and melting temperature

One of the main challenges when modeling density variations during solid-liquid phase change is that the volume of the PCM changes with time. In the case considered in the present work, water expands during solidification and, as it pushes against the elastic wall, the pressure inside the cavity rises. This pressure variation, in turn, changes the

melting temperature of the PCM, which results in the thermo-mechanical coupling between the PCM and the elastic wall. Depending on the value of the elastic wall spring constant, the pressure buildup will reach different levels, as shown in Fig. 10. At early times, the solidification rate is generally much higher and as a consequence, so is the expansion of the PCM. This is reflected in Fig. 10 by faster pressure rise at lower times. In can also be observed that, for the specific values of κ_w'' investigated in this paper, increasing the effective spring constant by one order of magnitude yields a pressure rise that is also of one order of magnitude.

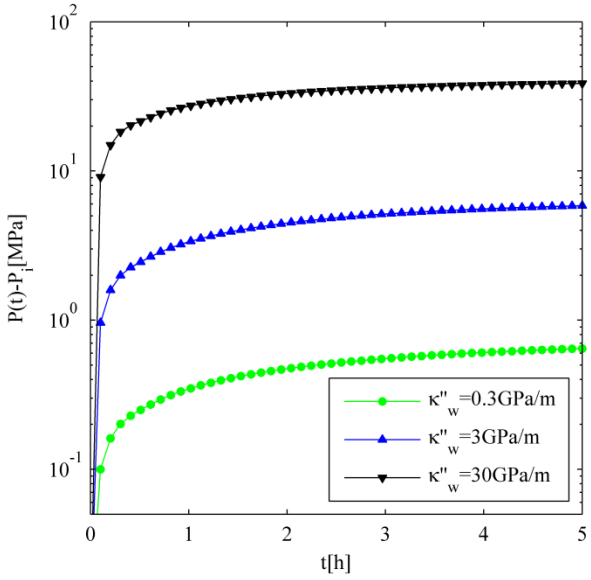

Figure 10

Figure 11 depicts the melting temperature of the PCM as a function of time for the different values of κ_w''. For the case of the lowest value of κ_w'', the pressure rise within the cavity was relatively small and as a consequence, the melting temperature of the PCM remained relatively close to the initial melting temperature (T_{mi} =0 ºC). However, as the value of κ_w'' is increased, the melting temperature decreases rapidly, especially for the highest value of κ_w''. Note that in the simulation with a top free ceiling and that with a constant density, the melting temperature simply stays equal 0 ºC at all time, which is why the melting temperature for these two reference cases was not shown explicitly in

Fig. 11. The temperature at which the density of liquid water is maximal ($T_{\max}$) is also shown for each value of κ_w'' in Fig. 11. It can be noted that for a given value of κ_w'', there will be a density extremum in the liquid phase inside the cavity if $T_m < T_{\max} < T_H$. By looking at Fig. 11, on can conclude that since $T_{\max}$ is larger than T_m during the entire simulation for κ_w''=0.3 and 3 GPa/m, there is always a density extremum inside the cavity. This was shown in Figs. 7 and 8 by the presence of two counter-rotating convective cells. On the opposite, Fig. 11 shows that $T_{\max}$ quickly drops below T_m for κ_w'' =30 GPa/m (i.e., there is no density extremum in the liquid phase after ~1 h). This explains why there was only one large convective cell inside the cavity in Fig. 9.

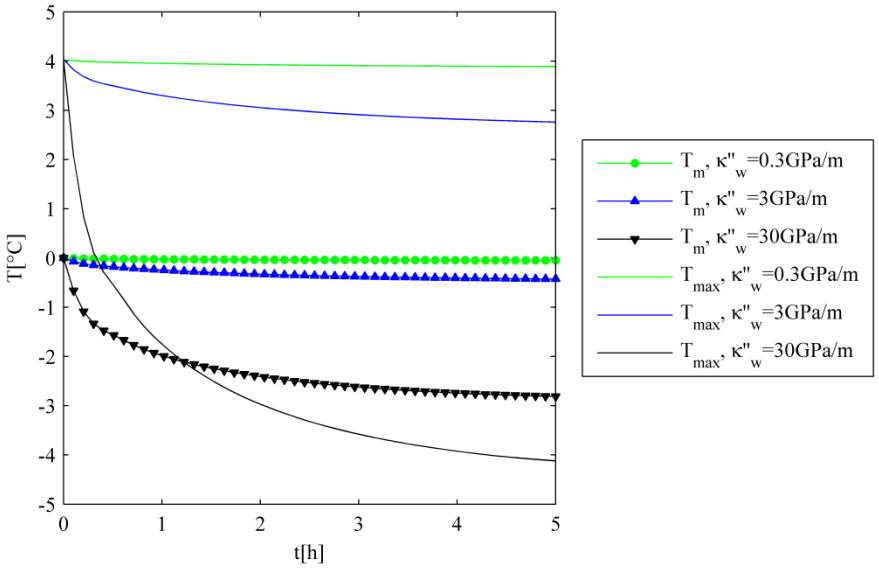

Figure 11

5.3 Thermal behavior of the system

Figure 12 depicts the solid-liquid interface position (defined as the position in the x direction at which $T = T_m$) at different times and for all aforementioned cases. As mentioned previously, conduction is the dominant mode of heat transfer at the beginning of the solidification process (t =15 min). As a result, the solid-liquid interface is mostly planar in all cases, as can be seen in Fig. 12a. When the effective spring constant $\kappa_w'' \neq 0$,

the pressure within the cavity builds up to different levels depending on the specific value of κ_w''. One of the consequences of this is the drop of the melting temperature as was shown in Fig. 11. When looking at Fig. 12 b-d, the solid-liquid interface positions for each case begin to differentiate as time progresses. It can be observed that the drop in melting temperature directly caused by the pressure rise inside the cavity hinders the solidification process and the position of the solid-liquid interface is slightly behind for higher values of the spring constant. This effect is more pronounced for the highest value of κ_w'' at t =300 min as seen in Fig. 12d. The differences in shape of the interfaces for each case are mainly caused by the different flow patterns as well as the relative shape, position, and size of the counter rotating convective cells in the liquid phase, as discussed previously.

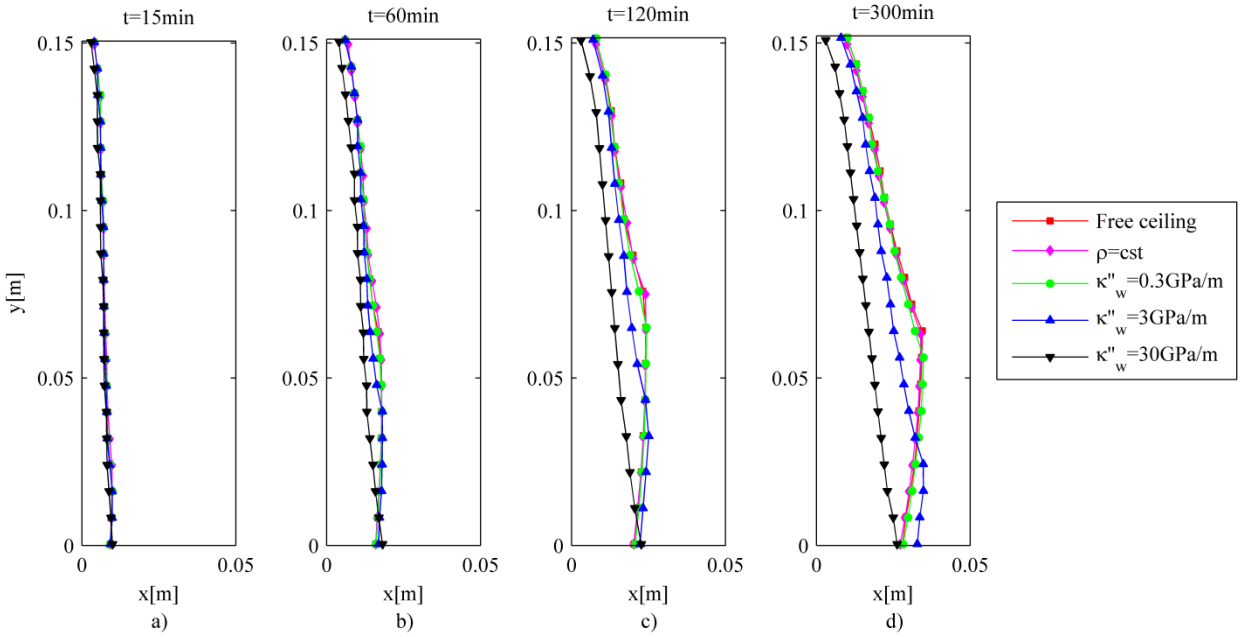

Figure 12

Even though the position of the interface is very similar at early times, see Fig. 12a, the temperature profiles are not. This is illustrated in Fig. 13 where the temperature profiles at t =15 min and at $y = H_i/10$ are shown for the three values of κ_w'', as well as for the free ceiling and constant density cases. Here, a solid gray line was added to the figure to show the range of the solid-liquid interface positions for the different cases. It

can first be observed that the temperature profiles in the solid phase are linear and very similar for all cases. On the other hand, significant differences can be observed in the liquid phase. The general shape of each curve is strongly influenced by the flow pattern inside the cavity (i.e., the number, shape, and size of convective cells), and by the temperature differential across the liquid phase (i.e., between the solidification front and the hot wall). Since both of these factors depend on the pressure rise in the cavity which varies depending on the case considered (e.g., $p - p_i$ =0.18, 1.80, and 16.68 MPa and $T_H - T_m$ =10.21, 10.33, and 11.42 ºC at t =15 min for κ_w'' =0.3, 3, and 30 GPa/m, respectively), it is thus expected that the flow pattern and, consequently, the temperature profiles be different in the liquid phase depending on the effective spring constant. It can also be seen that there are slight differences in the temperature profiles for the two reference cases (i.e., free ceiling and constant density). For the case where a free ceiling was modeled at the top of the cavity, the results are very close to the lowest value of κ_w'' since the free ceiling can essentially be seen as the limit case where the elastic wall's spring constant κ_w'' tends towards 0. The spring with a constant κ_w'' =0.3 GPa/m is not stiff enough to produce significantly different results compared to the free ceiling situation. Note, however, that there are larger differences in the temperature profile in the case of a constant density because using an average density between ρ_s and ρ_l instead of Eq. (5) changes the magnitude of the buoyancy forces driving natural convection in the melt and thus modifies the flow pattern.

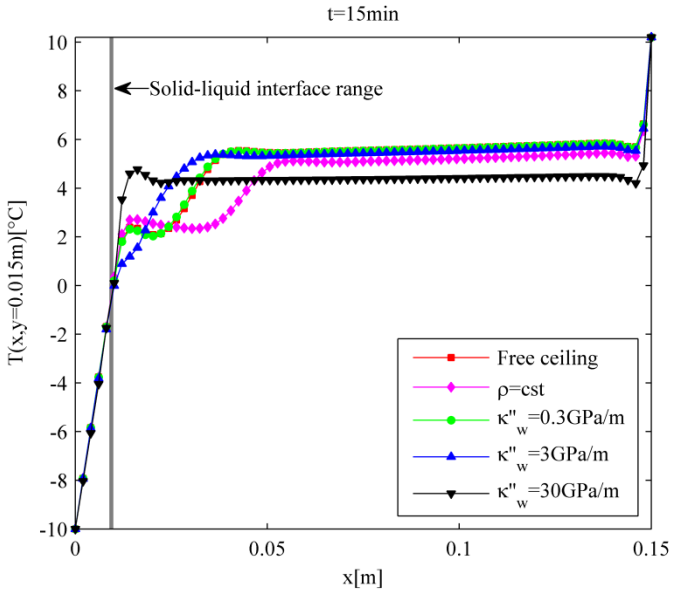

Figure 13

The average heat flux on each side of the cavity as a function of time is depicted in Fig. 14. It can first be noted that, in addition to heat being transferred from the hot side to the cold side by conduction and convection, latent heat extracted from the PCM during its solidification exits the cavity through the cold wall, which explains why the average heat flux is always higher at that wall. Soon after the beginning of the simulations, the large temperature difference between the PCM initially at T_i=10.2 ºC and the cold wall at T_C=-10 ºC results in high solidification rates and in rapidly increasing average heat fluxes through the lateral walls of the cavity, especially at the cold wall. However, as time passes, the growing layer of ice acts as a thermal insulation and it becomes more difficult to extract energy from the PCM. As a consequence, the solidification rate and the average heat fluxes across the lateral walls of the cavity decrease. If the PCM was allowed to solidify for a sufficiently long period of time, the system would eventually reach an equilibrium state where the average heat fluxes crossing the cold and hot walls would be equal. It can be observed in Fig. 14 that the pressure rise (and the corresponding drop of the melting temperature) hinders the solidification process. Indeed, the average heat fluxes are almost equal after 5h for κ''_w=30 GPa/m (system almost at equilibrium),

whereas the difference between the heat fluxes is larger for lower values of κ_w''. It can also be deduced from Fig. 14 that the average heat flux across the cavity at equilibrium would be higher for larger values of κ_w''.

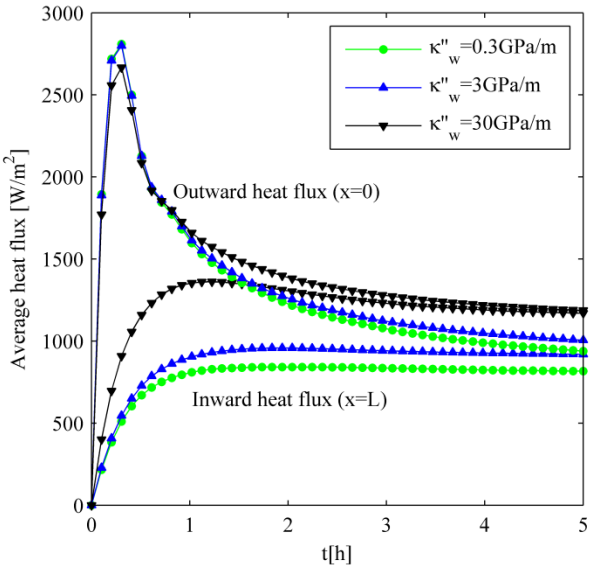

Figure 14

In order to illustrate the effect of the thermo-mechanical coupling on the overall solidification process, the solidified mass fraction (defined as the total mass of the solid phase normalized by the initial mass of the PCM) was plotted in Fig. 15. Note that the initial mass is the same in all cases except the case where the density is constant and equal to the average density of both phases. The case that yielded the highest solidified mass fraction after 300 min is the case with a constant density (17.24%). Indeed, less energy needs to be removed to solidify a given volume of liquid PCM in that case, as it contains less mass (the average density is lower than ρ_l). It was thus expected that the solidification rate would be higher in that specific case. When looking at the solidified mass fraction for the other reference case, i.e., free ceiling, it can be observed that it follows closely the lowest value of κ_w'' throughout the entire simulation. However, the solidified mass fraction is slightly higher for that reference case (16.21% for free ceiling at the end of the simulation as opposed to 16.07% for κ_w''=0.3 GPa/m) as there is no pressure rise inside the cavity that hinders solidification. For the other cases, Fig. 15 shows that the melting temperature drop associated with the pressure rise inside the

cavity directly results in a lower solidified mass fraction (14.56% and 9.62% for κ_w''=3 and 30 GPa/m, respectively).

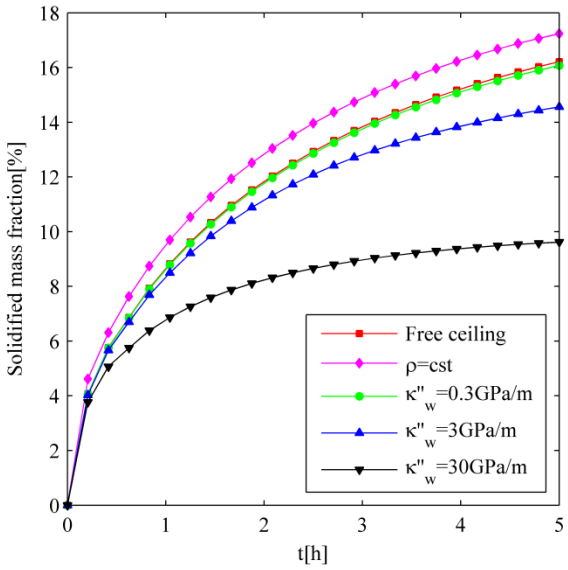

Figure 15

6. Conclusions

In the present paper, solidification of water near its density extremum while considering density variations during phase change was simulated. It was assumed that water resided inside a closed cavity with the top surface behaving as an elastic wall. A methodology was presented with the different adjustments required in order to implement the mathematical model in ANSYS Fluent 17.0. It was shown that the pressure rise inside the cavity as the PCM expands towards the elastic boundary influenced both the flow pattern and the solidification process at different levels. First, the melting temperature decreasing with pressure caused the solidification of water to slow down. This effect appeared to be more important for very large values of the spring constant (9.62% solidified mass fraction at the end of the simulation for κ_w''=30GPa/m as opposed to 16.21% for a free ceiling). In addition to affecting the solidified mass fraction at a given time, the thermo-mechanical coupling also influenced the dynamic process itself. Indeed, it was shown in Fig. 14 that although 5 h simulations were not long enough for the systems to reach equilibrium (regardless of the value of κ_w'' that was selected), the system with the highest effective spring constant was much closer to equilibrium than the system

with the lowest spring constant. It was also shown that even at early times when heat conduction is the main mode of heat transfer, some differences could be observed in the temperature profiles across the cavity, even though the position of the solid-liquid interface was very similar in all cases.

Significant differences were observed in the flow pattern, especially regarding the size of the two counter-rotating convective cells in the liquid phase. With the equation for the pressure-temperature dependent density used in the present work to express the buoyancy forces in the melt, the cold clockwise convective cell was found to shrink when the pressure inside the cavity increased due to larger values of κ_w''. When the spring constant was very large (which yielded the highest pressure rise inside the cavity), the cold convective cell would not form inside the cavity, which yielded a very different shape of the solidification front.

Although some validations were made against experiments, the full model could not be validated in such a way since, to the authors' knowledge, experimental results for a similar setup with thermo-mechanical coupling are not yet present in literature. Future work could focus on developing a test bench to measure heat transfer and flow patterns in closed cavities as the one studied in this paper. It would also be interesting to use and improve the thermo-mechanical model presented in this paper to perform simulations for a wider range of parameters, e.g., different initial and boundary conditions, cavity aspect ratios, geometries, use a pressure dependent latent heat of fusion, etc.

Acknowledgements

The authors' work is supported by the Natural Sciences and Engineering Research Council of Canada (NSERC).

References

[1] C.-J. Ho and R. Viskanta, "Inward solid-liquid phase-change heat transfer in a rectangular cavity with conducting vertical walls," *Int. J. Heat Mass Transf.*, vol. 27, no. 7, pp. 1055–1065, Jul. 1984.

[2] M. Okada, "Analysis of heat transfer during melting from a vertical wall," *Int. J. Heat Mass Transf.*, vol. 27, no. 11, pp. 2057–2066, Nov. 1984.

[3] Y. Wang, A. Amiri, and K. Vafai, "An experimental investigation of the melting process in a rectangular enclosure," *Int. J. Heat Mass Transf.*, vol. 42, no. 19, pp. 3659–3672, Oct. 1999.

[4] S. Wang, A. Faghri, and T. L. Bergman, "A comprehensive numerical model for melting with natural convection," *Int. J. Heat Mass Transf.*, vol. 53, no. 9–10, pp. 1986–2000, Apr. 2010.

[5] C. J. Ho, K. C. Liu, and W.-M. Yan, "Melting processes of phase change materials in an enclosure with a free-moving ceiling: An experimental and numerical study," *Int. J. Heat Mass Transf.*, vol. 86, pp. 780–786, Jul. 2015.

[6] C. Gau and R. Viskanta, "Melting and solidification of a pure metal on a vertical wall," *J. Heat Transf.-Trans. Asme*, vol. 108, no. 1, pp. 174–181, 1986.

[7] N. Kabei *et al.*, "A Thermal-Expansion-Type Microactuator with Paraffin as the Expansive Material. (Basic Performance of a Prototype Linear Actuator).," *JSME Int. J. Ser. C*, vol. 40, no. 4, pp. 736–742, 1997.

[8] L. Klintberg, M. Karlsson, L. Stenmark, J.-Å. Schweitz, and G. Thornell, "A large stroke, high force paraffin phase transition actuator," *Sens. Actuators Phys.*, vol. 96, no. 2–3, pp. 189–195, Feb. 2002.

[9] S. Ogden, L. Klintberg, G. Thornell, K. Hjort, and R. Bod?n, "Review on miniaturized paraffin phase change actuators, valves, and pumps," *Microfluid. Nanofluidics*, vol. 17, no. 1, pp. 53–71, Jul. 2014.

[10] C. J. Ho, W. J. Wang, and C.-M. Lai, "Dynamic response of a thermally activated paraffin actuator," *Int. J. Heat Mass Transf.*, vol. 103, pp. 894–899, Dec. 2016.

[11] J. Dallaire and L. Gosselin, "Various ways to take into account density change in solid–liquid phase change models: Formulation and consequences," *Int. J. Heat Mass Transf.*, vol. 103, pp. 672–683, Dec. 2016.

[12] E. Assis, L. Katsman, G. Ziskind, and R. Letan, "Numerical and experimental study of melting in a spherical shell," *Int. J. Heat Mass Transf.*, vol. 50, no. 9–10, pp. 1790–1804, May 2007.

[13] S. F. Hosseinizadeh, A. A. Rabienataj Darzi, F. L. Tan, and J. M. Khodadadi, "Unconstrained melting inside a sphere," *Int. J. Therm. Sci.*, vol. 63, pp. 55–64, Jan. 2013.

[14] H. Shmueli, G. Ziskind, and R. Letan, "Melting in a vertical cylindrical tube: Numerical investigation and comparison with experiments," *Int. J. Heat Mass Transf.*, vol. 53, no. 19–20, pp. 4082–4091, Sep. 2010.

[15] M. A. Hassab, M. M. Sorour, M. Khamis Mansour, and M. M. Zaytoun, "Effect of volume expansion on the melting process?s thermal behavior," *Appl. Therm. Eng.*, vol. 115, pp. 350–362, Mar. 2017.

[16] M.-J. Liu, L.-W. Fan, Z.-Q. Zhu, B. Feng, H.-C. Zhang, and Y. Zeng, "A volume-shrinkage-based method for quantifying the inward solidification heat transfer of a

phase change material filled in spherical capsules," *Appl. Therm. Eng.*, vol. 108, pp. 1200–1205, Sep. 2016.
[17] M. Conti, "Planar solidification of a finite slab: effects of the pressure dependence of the freezing point," *Int. J. Heat Mass Transf.*, vol. 38, no. 1, pp. 65–70, Jan. 1995.
[18] M. Conti, F. Marinozzi, and L. Papagno, "Pressure effects in the planar solidification of a finite slab: convective cooling and prescribed heat flux boundary conditions," *Il Nuovo Cimento C*, vol. 19, no. 2, pp. 257–270, Mar. 1996.
[19] W. Kowalczyk, C. Hartmann, and A. Delgado, "Modelling and numerical simulation of convection driven high pressure induced phase changes," *Int. J. Heat Mass Transf.*, vol. 47, no. 5, pp. 1079–1089, Feb. 2004.
[20] Y.-C. Yen, "Review of Thermal Properties of Snow, Ice and Sea Ice (CRREL Report 81-10)," U.S. Army Cold Regions Research and Engineering Laboratory, Hanover, NH, 1981.
[21] "ANSYS® Fluent, Release 17.0, Help System, Theory Guide, Ansys, Inc." .
[22] F. P. Incropera, D. P. DeWitt, T. L. Bergman, and A. S. Lavine, *Fundamentals of Heat and Mass Transfer*, 6th ed. John Wiley & Sons, Inc., 2007.
[23] B. Gebhart and J. C. Mollendorf, "A new density relation for pure and saline water," *Deep Sea Res.*, vol. 24, no. 9, pp. 831–848, Sep. 1977.
[24] A. Bejan, *Convection Heat Transfer, 4th Edition*, 4th ed. John Wiley & Sons, Inc., 2013.
[25] P. C. Carman, "Fluid flow through granular beds," *Chem. Eng. Res. Des.*, vol. 75, pp. S32–S48, Dec. 1997.
[26] A. C. Kheirabadi and D. Groulx, "SIMULATING PHASE CHANGE HEAT TRANSFER USING COMSOL AND FLUENT: EFFECT OF THE MUSHY-ZONE CONSTANT," *Comput. Therm. Sci. Int. J.*, vol. 7, no. 5–6, pp. 427–440, 2015.
[27] R. Dyja, E. Gawronska, A. Grosser, P. Jeruszka, and N. Sczygiol, "Estimate the Impact of Different Heat Capacity Approximation Methods on the Numerical Results During Computer Simulation of Solidification," *Eng. Lett.*, vol. 24, no. 2, pp. 237–245, 2016.
[28] "ANSYS® Fluent, Release 17.0, Help System, User's Guide, Ansys, Inc." .
[29] J. Dallaire and L. Gosselin, "Solid-Liquid Phase Change with Variable Density: Formulation of Conservation Equations with Enthalpy Methods," *Int. J. Therm. Sci.*, Under review.
[30] M. N. Ozisik, *Heat Conduction*, 2nd Edition. Wiley-Interscience, 1993.
[31] S. L. Braga and R. Viskanta, "Effect of density extremum on the solidification of water on a vertical wall of a rectangular cavity," *Exp. Therm. Fluid Sci.*, vol. 5, no. 6, pp. 703–713, Nov. 1992.
[32] T. J. Scanlon and M. T. Stickland, "A numerical analysis of buoyancy-driven melting and freezing," *Int. J. Heat Mass Transf.*, vol. 47, no. 3, pp. 429–436, Jan. 2004.
[33] S. L. Braga and R. Viskanta, "Transient natural convection of water near its density extremum in a rectangular cavity," *Int. J. Heat Mass Transf.*, vol. 35, no. 4, pp. 861–875, Apr. 1992.
[34] R. T. Tenchev, J. A. Mackenzie, T. J. Scanlon, and M. T. Stickland, "Finite element moving mesh analysis of phase change problems with natural convection," *Int. J. Heat Fluid Flow*, vol. 26, no. 4, pp. 597–612, Aug. 2005.

Figure captions

Figure 1 Schematic representation of the domain under study

Figure 2 Equivalent specific heat as a function of temperature to account for latent heat

Figure 3 Comparison of the solid-liquid interface position as a function of time with the present model and the analytical solution to the Stefan problem [30]

Figure 4 Comparison of the phase change interface over time in a cavity with gallium in the presence of buoyancy forces from the present model and that of [6]

Figure 5 Comparison of the phase change interface over time in a cavity filled with water near its density extremum from the present model and that of [31]

Figure 6 Validation of the thermo-mechanical coupling in the present model with the model in [11], a) Position of the solid-liquid interface and b) Melting temperature

Figure 7 Contours of a) the stream function and b) temperature at t =300 min for κ_w'' =0.3 GPa/m

Figure 8 Contours of a) the stream function and b) temperature at t =300 min for κ_w'' =3 GPa/m

Figure 9 Contours of a) the stream function and b) temperature at t =300 min for κ_w'' =30 GPa/m

Figure 10 Pressure rise as a function of time for different values of κ_w''

Figure 11 Melting temperature (T_m) and temperature at which the density of water is maximal ($T_{\max}$) as a function of time for different values of κ_w''

Figure 12 Position of the solid-liquid interface at different times; a) t =15 min, b) t =60 min, c) t =120 min, and d) t =300 min

Figure 13 Temperature profile at t =15 min and $y = H_i/10$ for different values of κ_w''

Figure 14 Average heat flux on each side of the cavity as a function of time

Figure 15 Solidified mass fraction as a function of time

Table captions

Table 1 Physical properties of water and ice